JOURNAL OF COLLOID AND INTERFACE SCIENCE **192,** 350–362 (1997)
ARTICLE NO. CS975018

A Theoretical Study of Instabilities at the Advancing Front of Thermally Driven Coating Films

Dawn E. Kataoka and Sandra M. Troian[1]

Department of Chemical Engineering, Princeton University, Princeton, New Jersey 08544-5263

Received February 18, 1997; accepted June 2, 1997

A thin liquid coating can spread vertically beyond the equilibrium meniscus position by the application of a temperature gradient to the adjacent substrate. So called super-meniscus films experience a surface shear stress which drives flow toward regions of higher surface tension located at the cooler end of the substrate. The Marangoni stresses responsible for this spreading process can also be used to coat horizontal surfaces rapidly and efficiently. Experiments in the literature have shown that in either geometry, the advancing front can develop a pronounced ridge with lateral undulations that develop into long slender rivulets. These rivulets, which prevent complete surface coverage, display a remarkable regularity in height, width, and spacing which suggests the presence of a hydrodynamic instability. We have performed a linear stability analysis of such thermally driven films to determine the most dangerous wavenumber. Our numerical solutions indicate the presence of an instability at the advancing front of films which develop a sufficiently thick capillary ridge. Our results for the film thickness profiles and spreading velocities, as well as the wavenumber corresponding to the most unstable mode, compare favorably with recent experimental measurements. An energy analysis of the perturbed flow reveals that the increased mobility in the thickened portions of the films strongly promotes unstable flow, in analogy with other coating processes using gravitational or centrifugal forces.

Key Words: **fingering instability; Marangoni stress; coating flows; capillarity.**

INTRODUCTION

Coating processes normally require an external driving force to spread a liquid film along a solid substrate. Tilting or spinning a substrate can provide the necessary body force to coat a substrate rapidly and efficiently. For situations in which the substrate cannot be moved or readily accessed, surface forces can be manipulated to drive the spreading process. For example, thermal gradients provide an especially useful way to direct thin films into small crevices requiring lubrication. A liquid film supported on a substrate subject to a thermal gradient will experience a varying surface tension depending on the local temperature since colder regions of the air–liquid interface maintain a higher surface tension than the warmer regions. A thin liquid film in contact with a vertical substrate to which is applied a temperature gradient will experience a surface shear stress. This thermally induced Marangoni stress will force the liquid to spread vertically beyond the equilibrium meniscus region and form a super-meniscus film (1).

The growing interest in micromachinery and lubrication phenomena has spawned many studies of thin interfacial films subject to surface forces. In cases where the liquid surface to volume ratio is significant, even small surface forces can create unusual flow patterns and large flow velocities. Over the years, several experiments have examined the spreading of thin nonvolatile films driven by a constant surface shear stress. Thermally induced flow has been investigated in both vertical (1–3) and horizontal (4) geometries. ''Blowing off films,'' which are driven by the action of an air stream moving over the free surface to create a surface shear stress, have also been studied (5) and used (6, 7) as a technique for measuring the viscosity of Newtonian and non-Newtonian films. Recent observations of silicone oil spreading on a silicon wafer in either a vertical (2, 3) or horizontal (4) geometry have shown the development of a pronounced ridge at the advancing front with lateral undulations which develop into long slender rivulets, as shown in Fig. 1. These experiments indicate the presence of a hydrodynamic instability at the advancing edge. Earlier studies of thermally driven squalane films spreading along a vertical silver plate, however, observed no ridge at the advancing front and no rivulet formation, despite careful observations of the climbing film at the leading edge (1). Measurements of the film thickness at the advancing front showed that upon approach to the moving front, the film thickness decreased smoothly and monotonically toward the substrate. These smooth profiles produced uniform and complete surface coverage, unlike the rivulets detected in the later studies. Since these systems all involve fluids known to wet completely the substrates on which they were spread, the results seem inconsistent. Our analysis shows that both scenarios are possible depending on the strength of the driving force and the

[1] To whom correspondence should be addressed.

0021-9797/97 $25.00

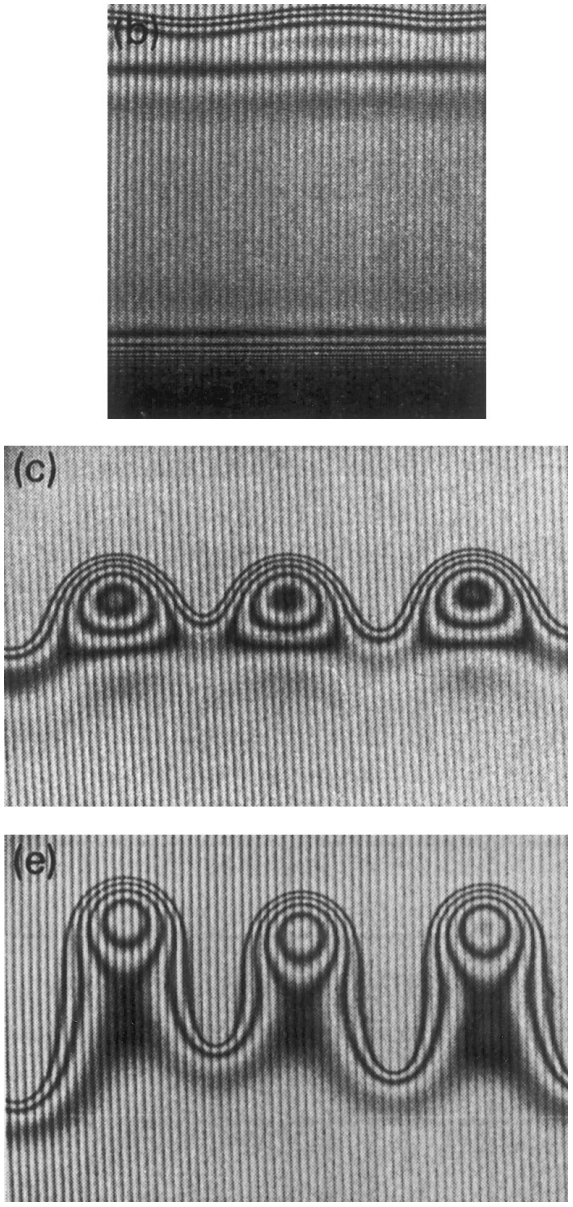

FIG. 1. Time development of the fingering instability of a climbing silicone oil film on a silicon wafer. Illustration reproduced from Cazabat *et al.* (19).

thickness of any prewetting film ahead of the nominal contact line.

In this paper, we examine coating flows driven by a shear stress created by a linear temperature profile applied to a supporting substrate. We consider the case of a constant shear stress for direct comparison with experiments reported in the literature. The formalism can easily be extended to cases of nonuniform stress. Within the lubrication approximation, we separate the flow into two regimes: an outer region far from the leading edge driven by the balance between viscous and Marangoni forces, and an inner region close to the leading edge in which capillary forces due to strong curvature also become significant. For sufficiently thin films or sufficiently large shear stresses, gravitational forces are negligible, in which case both vertical and horizontal geometries can be treated simultaneously. The film profiles and spreading velocities in the outer region allow a simple analytic form. Our numerical results of the film thickness in the inner region indicate the presence of a pronounced capillary ridge for sufficiently strong Marangoni stresses or sufficiently small precursor film thicknesses. The stability of this capillary region can be studied in direct analogy to other forced spreading problems driven by body forces such as gravity (8) or centrifugation (9). A linear stability analysis predicts the most unstable wavenumber and establishes a correlation between the presence of a capillary ridge and subsequent finger-like protrusions at the advancing front. Decreasing the amplitude of the capillary ridge promotes stability. Following Spaid and Homsy (9), we perform an energy analysis which demonstrates that the increased mobility in the thickened portions of the films strongly promotes unstable flow, in agreement with their previous analysis of spin coating flows. Finally, we compare our predictions to the squalane experiments of Ludviksson and Lightfoot (1) and the silicone oil studies of Cazabat and co-workers (2, 3) and Brzoska *et al.* (4) to reconcile experimental discrepancies and to highlight which parameters should be measured to make direct comparison with the theoretical model. A careful examination of all available experimental data reveals that a monotonically decreasing film thickness produces uniform and stable flow, whereas the presence of a ridge produces an instability at the moving front. Such comparison furthers understanding of the mechanisms responsible for the frontal instability and can be used to design smoother and more uniform coatings by suppressing the formation of rivulets.

PROBLEM FORMULATION

We consider the flow of a thin Newtonian liquid film spreading along the surface of a solid substrate to which is applied a constant temperature gradient along the direction of flow. This temperature gradient produces a constant shear stress at the air–liquid interface of the adjacent liquid. In addition to this surface shear stress, there may also exist gravitational forces, which may induce drainage, or hydrostatic forces, which may induce film leveling. Within the lubrication approximation, the equations of motion reduce to

$$\eta \frac{\partial^2 u}{\partial z^2} = \frac{\partial p}{\partial x} + \rho g \sin \theta \qquad [1]$$

$$\eta \frac{\partial^2 v}{\partial z^2} = \frac{\partial p}{\partial y} \qquad [2]$$

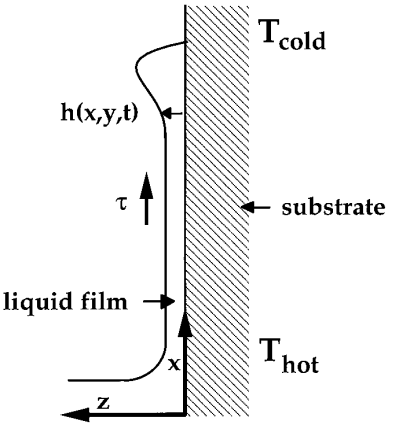

FIG. 2. Schematic of spreading geometry for vertically climbing films.

$$\frac{\partial p}{\partial z} = 0, \qquad [3]$$

where x represents the direction of the flow, y the direction transverse to the flow, and z the direction perpendicular to the substrate. The schematic for $\theta = \pi/2$ is shown in Fig. 2, where θ represents the angle of inclination of the substrate from the horizontal. The velocity components u and v represent flow in the x and y directions and p denotes the local pressure in the film, whose surface is located at $z = h(x, y, t)$. The liquid viscosity, density, and local surface tension are given by η, ρ, and γ, respectively, and g denotes the gravitational constant. In what follows the applied temperature gradient produces variations in surface tension which are much larger than the variations produced in the fluid density or viscosity. The density and viscosity of the coating film are therefore held constant. In addition, typical estimates appropriate to natural convection in the air above the liquid film indicate that the Biot number is extremely small, in which case the heat transfer across the liquid film is minimal. The temperature profile at the liquid film surface is therefore assumed to be the temperature profile of the solid substrate. We solve the lubrication equations subject to the boundary conditions of no-slip at the solid surface

$$u, v|_{z=0} = 0, \qquad [4]$$

and constant shear stress, $\tau = (d\gamma/dT)(dT/dx)$, at the air–liquid interface

$$\eta \left.\frac{\partial u}{\partial z}\right|_{z=h} = \tau. \qquad [5]$$

Since $d\gamma/dT$ is a constant for most liquids, application of a linear temperature profile ensures a constant surface shear stress. Likewise, a gas stream blowing across the surface of a thin liquid film to produce a constant shear stress can also be described by the same equations and boundary conditions. For regions of the flow in which capillary forces are significant, the pressure gradient induced by surface curvature is given by $\nabla p_{\text{cap}} = -\nabla(\gamma\nabla^2 h)$ in the limit of small slopes. The total pressure gradient, including any hydrostatic effects, is given by $\nabla p = \nabla(-\gamma\nabla^2 h + \rho g h \cos\theta)$. The resulting height-averaged velocities are

$$U(x, y) = \frac{\tau h}{2\eta} + \frac{h^2}{3\eta}\frac{\partial}{\partial x}(\gamma\nabla^2 h - \rho g h \cos\theta) - \frac{\rho g h^2 \sin\theta}{3\eta} \qquad [6]$$

$$V(x, y) = \frac{h^2}{3\eta}\frac{\partial}{\partial y}(\gamma\nabla^2 h - \rho g h \cos\theta). \qquad [7]$$

The film thickness profiles can be determined by substituting the velocities into the interface equation

$$\frac{\partial h}{\partial t} + \frac{\partial}{\partial x}(hU) + \frac{\partial}{\partial y}(hV) = 0. \qquad [8]$$

Gravitational effects are negligible for film thicknesses $h \ll \tau/(\rho g \sin\theta)$ if drainage is present ($\theta > 0$) or $h\epsilon \ll \tau/(\rho g \cos\theta)$ if hydrostatic forces are present ($\theta < \pi/2$). The lubrication parameter $\epsilon = h_c/L_c \ll 1$, where h_c represents the characteristic film thickness and L_c the characteristic extent of the spreading film in either the x or y direction. The height-averaged velocities for films satisfying these conditions become

$$U(x, y) = \frac{\tau h}{2\eta} + \frac{h^2}{3\eta}\frac{\partial}{\partial x}(\gamma\nabla^2 h) \qquad [9]$$

$$V(x, y) = \frac{h^2}{3\eta}\frac{\partial}{\partial y}(\gamma\nabla^2 h). \qquad [10]$$

For regions of the flow in which capillary forces are negligible, the velocity profile in the x direction reduces to planar Couette flow.

Outer Region

Marangoni forces and capillary forces exert their influence over different length scales. On length scales, L_c, comparable to the extent of the spreading film, capillary effects are negligible provided

$$\frac{\gamma h_c^2}{\tau L_c^3} \sim \frac{\gamma}{\Delta\gamma}\epsilon^2 \ll 1, \qquad [11]$$

where $\tau \sim \Delta\gamma/L_c$ and $\Delta\gamma$ is the change in surface tension

over the length scale L_c. Since $\gamma/\Delta\gamma$ is a quantity of order one for most liquids, this inequality is easily satisfied in the lubrication approximation. In this outer region it is the balance between the Marangoni driving force and the viscous retardation effects due to the no slip condition at the substrate that sets the characteristic velocity for the spreading film,

$$U_c = \frac{\tau h}{2\eta}. \qquad [12]$$

Substitution of Eq. [12] into Eq. [8] yields the interface equation for the film thickness,

$$h_t + \frac{\tau}{\eta} h h_x = 0, \qquad [13]$$

which can be solved by the method of characteristics to give

$$x = x_*(h) + \frac{\tau h}{\eta} t. \qquad [14]$$

The quantity $x_*(h)$ represents the initial value of a characteristic. Equation [14] can therefore be inverted to obtain the film thickness

$$h = \frac{\eta}{\tau}\left[\frac{x - x_*}{t}\right], \qquad [15]$$

which, for sufficiently long times when memory of initial conditions is erased, assumes the self-similar form

$$h \to \frac{\eta}{\tau}\left[\frac{x}{t}\right]. \qquad [16]$$

For a finite reservoir of spreading fluid of constant width in the transverse flow direction, the global mass balance dictates that

$$\int_0^{x_N(t)} h(x, t)dx = A, \qquad [17]$$

where $x_N(t)$ denotes the downstream edge of the film and A the cross-sectional area of fluid in the x–z plane. Substitution of the self-similar profile into Eq. [17] gives the position of the leading edge of the film for the outer region,

$$x_N = \left(\frac{2A\tau}{\eta}\right)^{1/2} t^{1/2}. \qquad [18]$$

Inner Region

Equation [16] indicates that the film assumes a ramp profile which ends abruptly and achieves its maximum height at the leading edge of the outer region. An inner region therefore exists in which this film height must smoothly decrease to meet the substrate. This decrease in film thickness will involve significant curvature such that capillary forces must be included as part of the force balance. The pressure gradient in the inner region is therefore nonnegligible and of the form $\nabla p_{cap} = -\nabla(\gamma\nabla^2 h)$. The term on the right-hand side involves gradients of the surface tension, γ, as well as gradients in the curvature, $\nabla^2 h$; however, the gradient in surface tension is of order $d\gamma/dx \sim \Delta\gamma/L_c$, whereas the gradient in curvature is of order h/l^3, where l represents the much smaller scale of the inner region which we define in Eq. [20]. The pressure gradient which couples curvature effects to gradients in surface tension can therefore be ignored at the scale of the inner region with the result that the total pressure gradient throughout the film is

$$\nabla p = -\gamma\nabla(\nabla^2 h). \qquad [19]$$

A scaling analysis of Eq. [9] determines the extent of the inner region which represents the length scale over which Marangoni forces, viscous forces, and capillary forces balance, namely,

$$l = h_N(3Ca)^{-1/3}, \qquad [20]$$

where h_N is the film thickness at the leading edge of the outer region, $Ca = \eta U_N/\gamma$ is the capillary number, and U_N is the height-averaged velocity in the downstream direction evaluated at h_N. As we shall see, the flow in the inner region requires only the value of the film thickness, h_N, to set the scale of the incoming fluid flux. Many different coating problems can therefore be modeled in the same fashion. The leading edge of thin spreading films driven by gravity as in falling films, by centrifugation as in spin coating problems, or by surface shear stresses as in super-meniscus films or blowing off films can all be modeled identically in the inner region where a force balance exists between the driving force for spreading, capillarity, and viscous retardation (8–11).

To solve for the flow near the leading edge, we first rescale the variables in Eqs. [8]–[10] according to the characteristic scales in the inner region. The film thickness is rescaled by h_N, time is rescaled by l/U_N, and the velocity fields, U and V, are rescaled by U_N. We stretch our inner coordinates to be $\xi = -x/l$ and $\zeta = y/l$ and solve the resulting dimensionless equation subject to the asymptotic boundary conditions behind and ahead of the leading edge. For convenience, we have reversed our coordinate system such that the inner region matches onto the outer region as $\xi \to +\infty$. The film thickness in the inner region must smoothly match onto the film thickness h_N.

The boundary condition as $\xi \to -\infty$ requires some discussion. It is well known that adherence to the no slip boundary

condition in situations involving the spreading of a liquid on a solid will produce a singularity in the stress at the position of the moving contact line, defined as the position where the liquid meets the solid substrate. Singularities of the flow often signal some breakdown in the assumptions of the model. Two different approaches have been used to alleviate this mathematical problem for cases of liquid-on-solid spreading. The first approach requires the use of some phenomenological slip boundary condition near the contact line (12, 13). Several models have been proposed in the literature, and each share the feature that the singularity is removed by somehow preventing the liquid molecules from actually sticking to the solid substrate. The second approach, which we follow, assumes the existence of a precursor film beyond the nominal contact line (14, 15). This precursor film can be purposely coated onto a substrate or develop naturally as a result of evaporation/condensation processes or surface diffusion occurring at the advancing front of the spreading film. The thickness of this precoating film can therefore assume macroscopic to microscopic dimensions, but in either case, its presence conveniently removes the singularity at the contact line. Of course, beyond this precursor film one encounters the same difficulty at the new position of the contact line (which is usually relieved by a slip condition), but the singularity at the original position of the contact line has been removed. Previous studies of driven spreading problems have shown that both the base flow and perturbed profiles are relatively insensitive to the approach taken, be it the slip or precursor film model (9, 16). The asymptotic boundary condition in the inner region therefore requires that the film thickness smoothly matches onto the precursor film thickness, bh_N, as $\xi \to -\infty$.

Substituting the expressions for the velocity, [9] and [10], into Eq. [8] and employing the scalings introduced above yield the dimensionless interface equation for the inner region,

$$h_t - [h^2 - h^3(\nabla^2 h)_\xi]_\xi + [h^3(\nabla^2 h)_\zeta]_\zeta = 0, \quad [21]$$

where $\nabla^2 = \partial_{\xi\xi} + \partial_{\zeta\zeta}$. In general, the solution to Eq. [21] must satisfy four boundary conditions in ξ, four boundary conditions in ζ, and one initial condition. The absence of any explicit dependence on ξ and ζ implies that the solutions for h are translationally invariant in the ξ and ζ directions.

RESULTS

Base Flow

To solve for the film thickness profile, we postulate a one-dimensional traveling wave solution for the unperturbed flow of the form $h_0(\xi + ct)$, which incurs an infinitesimal two-dimensional exponential disturbance, $h_1(\xi + ct, \zeta, t)$, according to

$$h(\xi, \zeta, t) = h_0(\xi + ct) + h_1(\xi + ct, \zeta, t). \quad [22]$$

Substitution of this first-order expansion into Eq. [21] yields an ordinary differential equation for the base flow profiles,

$$ch_{0\xi} - (h_0^2)_\xi + (h_0^3 h_{0\xi\xi\xi})_\xi = 0, \quad [23]$$

which, when integrated once and subject to the four boundary conditions

$$h_0 \to 1 \text{ and } h_{0\xi\xi\xi} \to 0 \quad \text{as} \quad \xi \to \infty \quad [24]$$

$$h_0 \to \text{b} \text{ and } h_{0\xi\xi\xi} \to 0 \quad \text{as} \quad \xi \to -\infty, \quad [25]$$

yields the base flow equation

$$h_{0\xi\xi\xi} = \frac{b}{h_0^3} - \frac{1+b}{h_0^2} + \frac{1}{h_0}. \quad [26]$$

Moriarty *et al.* (11) previously solved this equation, which also arises in spray coating applications, by using the method outlined by Tuck and Schwartz (16) in which a third-order equation is converted into three first-order equations and solved as an initial value problem. The initial value is derived by linearizing Eq. [26] about the asymptotic value $h_0 \to 1$ as $\xi \to +\infty$ to give the form

$$h_0 \to 1 + a\exp(-\alpha\xi)\cos(\alpha\sqrt{3}\xi) \text{ as } \xi \to \infty, \quad [27]$$

where $\alpha = (1-b)^{1/3}/2$ and a is a small parameter about which the solution is iterated until convergence is achieved so that $h_0 \to b$ as $\xi \to -\infty$. When actually employing the expansion about h_0, the second-order term proportional to a^2 is also retained to further strengthen the initial value for numerical integration. As observed in other coating problems (11), it is not actually possible in practice to prevent the solution for h_0 from diverging as $\xi \to -\infty$ since the exponentially growing solution near $h_0 \to b$ begins to create numerical divergences. Fortunately, one can solve for a finite and self-consistent solution to seven digit accuracy in the parameter a before the numerical instability is established. The numerical solution requires a nonuniform mesh to treat properly regions of the flow where the film thickness exhibits rapid variation in height and curvature. Solutions to Eq. [26] for precursor film thicknesses ranging from $b = 0.01$ to $b = 0.90$ are plotted in Figs. 3a and 3b. It becomes increasingly more difficult to investigate smaller values of b because the exponentially growing solution begins to diverge even closer to the position where the fluid wedge joins the precursor film. The range of values explored, however, accurately captures all of the important features of the base flow and its stability characteristics. A significant feature of the film profiles is that the amplitude of the capillary ridge decreases as the precursor film thickness increases.

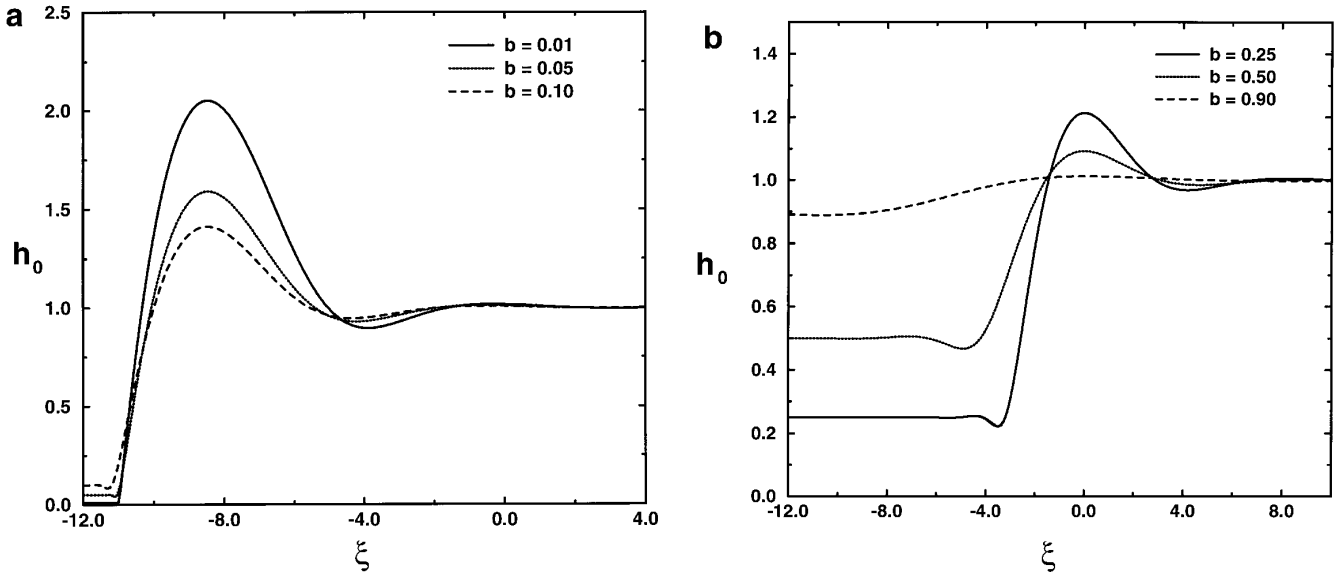

FIG. 3. Base flow film profiles of the inner region for small (a) and large (b) precursor film thicknesses.

Linear Stability Analysis

Since Eq. [21] is fully separable in ξ, ζ, and t, we seek solutions to the next order, h_1, which are periodic in ζ and exponential in time. The normal mode form for the disturbance becomes

$$h_1(\xi + ct, \zeta, t) = G(\xi + ct)\exp(iq\zeta + \beta t), \quad [28]$$

where q is the dimensionless wavenumber and β is the growth rate of the perturbation. The resulting eigenvalue equation for the disturbance function G is

$$\beta G + (1 + b)G_\xi - \frac{\partial}{\partial \xi}[2h_0 G - 3h_0^2 h_{0\xi\xi\xi} G - h_0^3(G_{\xi\xi\xi} - q^2 G_\xi)] + h_0^3(q^4 G - q^2 G_{\xi\xi}) = 0, \quad [29]$$

which must satisfy the four boundary conditions

$$G, G_\xi \to 0 \quad \text{as} \quad \xi \to \pm\infty. \quad [30]$$

As observed in other driven spreading problems, if the base flow h_0 were perfectly flat everywhere, integrating Eq. [29] once and applying the decay boundary conditions to all higher derivatives of G would yield $\beta = -q^4 h_0^3$. The eigenvalue β would therefore always be negative implying stable flow for any wavenumber disturbance. It is therefore the complex spatial structure of h_0, as shown in Figs. 3a and 3b, that gives rise to unstable flow.

Equation [29] was discretized using a central difference scheme with a nonuniform mesh such that regions of rapid variation in the base flow are accurately represented. The solutions for thin precursor films require more mesh points since the base flows display significant curvature upon approach to the precursor film. The eigenvalues and eigenfunctions of the discretized equations were calculated using RGG, a standard QR algorithm in the EISPACK library (17). In Fig. 4a we plot the dispersion curves, $\beta(q)$, for relatively thin precursor films. The eigenvalue β is positive over a range of wavenumbers indicating that the base flow is linearly unstable to disturbances in this regime. The thinnest precursor film investigated, namely $b = 0.01$, yields the largest eigenvalue at a wavenumber corresponding to $q_{\max} \approx 0.35$. Varying the precursor film thickness by a factor of 25 does not change this maximally growing wavenumber by more than roughly 10%. This value of $q_{\max}$ corresponds to a dimensional wavelength $\lambda \approx 18l$. The dispersion curves for thicker precursor films in the range $b \geq 0.25$ are illustrated in Fig. 4b. In contrast to spreading films with thin precursor layers, films with very thick precursor layers of order $b \geq 0.5$ are linearly stable to all wavenumbers. This result clearly illustrates that thicker precursor films promote stable spreading.

Figure 5 illustrates the shape of the eigenfunction corresponding to a range of unstable wavenumbers for $b = 0.10$. This disturbance function is localized precisely in the region where the base flow solution decreases from its maximum value to match smoothly onto the precursor film. Smaller values of b cause the function G to become even steeper near the advancing front and to narrow slightly in width. This sharpening effect is directly correlated to the larger value of $h_{0\xi\xi\xi}$ experienced at the advancing front of the base flow for spreading over thin precursor films. To visualize the full linearized solution to the spreading problem, we have

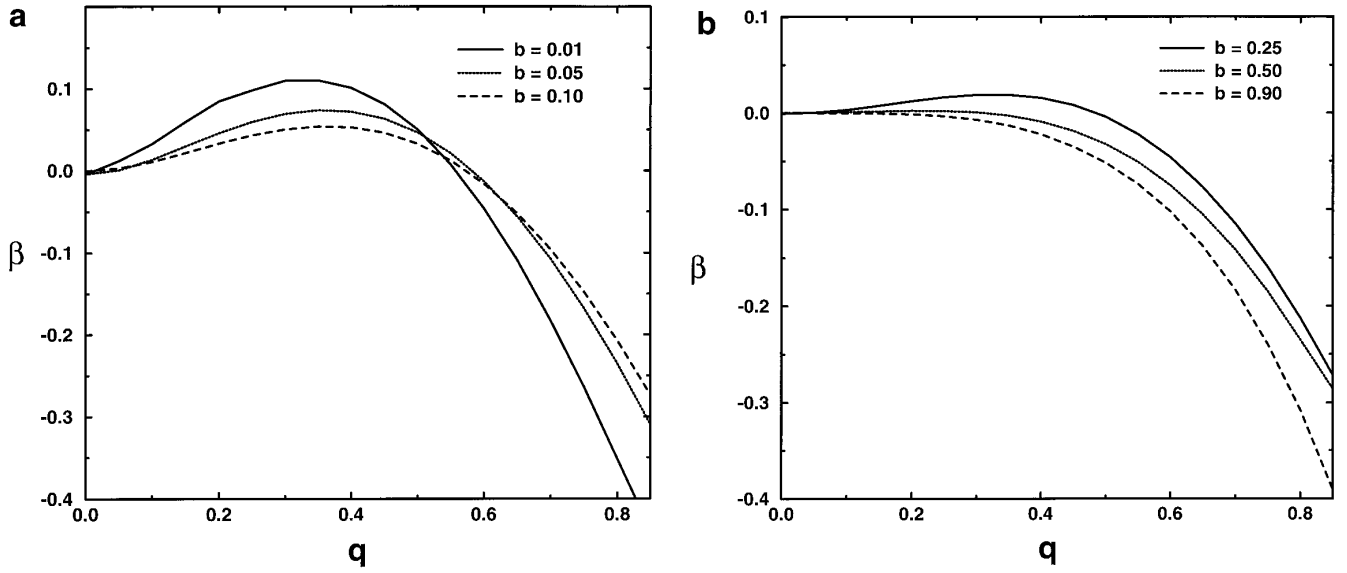

FIG. 4. Dispersion curve as a function of wavenumber q for small (a) and large (b) precursor film thicknesses.

extended the most unstable mode for $b = 0.10$ periodically in the ζ direction and superimposed this disturbance onto the base flow, as shown in Fig. 6. The magnitude of the disturbance has been exaggerated somewhat to illustrate the incipient rivulet formation. To capture the rivulet formation at later stages, one needs to solve the full, nonlinear equation [21], a problem for future investigation. Although the linear stability analysis has demonstrated the conditions for which a thermally driven film can experience an instability at the advancing front, we cannot conclude simply from the shape of the disturbance what physical mechanisms give rise to unstable flow. The following energy analysis clearly elucidates the two mechanisms responsible.

Energy Analysis

Following the method outlined by Spaid and Homsy (9), who examined the stability of flows driven by centrifugation, we seek to determine the destabilizing mechanisms leading to rivulet formation in thermally driven films. This analysis examines each term in the disturbance equation [29] to determine whether it contributes or removes energy from the

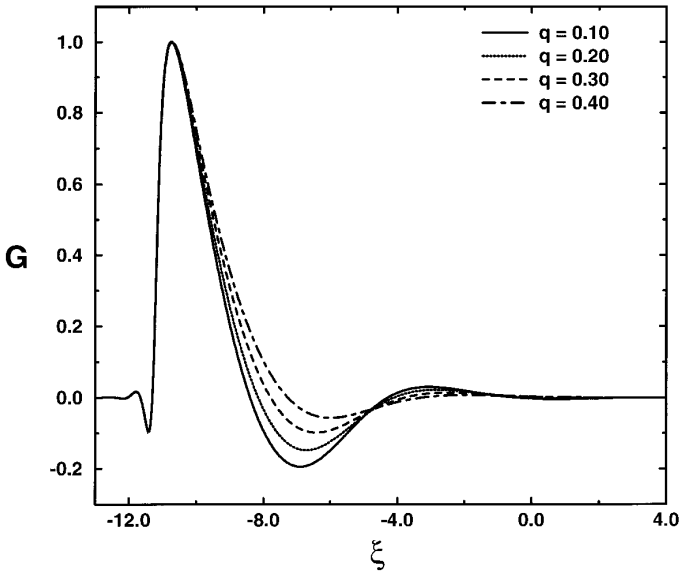

FIG. 5. Eigenfunction G corresponding to the largest eigenvalue for a dimensionless precursor film thickness of $b = 0.10$.

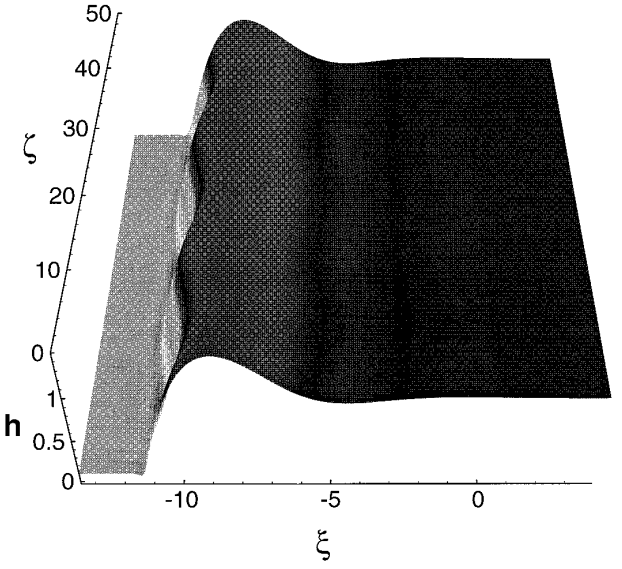

FIG. 6. Illustration of the onset of instability. The eigenfunction of the most unstable mode is superimposed upon the base flow profile for a dimensionless precursor film thickness of $b = 0.10$.

TABLE 1
Terms and Corresponding Mechanisms Involved in Energy Analysis

Term	Expression	Physical mechanism
1	$(1 + b)G_\xi$	Convective flow in ξ direction due to traveling wave reference velocity
2	$\partial/\partial\xi(h_0^3 G_{\xi\xi\xi})$	Capillary flow in ξ direction induced by perturbation curvature in ξ
3	$-\partial/\partial\xi(q^2 h_0^3 G_\xi)$	Capillary flow in ξ direction induced by perturbation curvature in ζ
4	$-\partial/\partial\xi(2Gh_0)$	Marangoni flow in ξ direction due to perturbation thickness variations
5	$\partial/\partial\xi(3Gh_0^2 h_{0\xi\xi\xi})$	Capillary flow in ξ direction due to perturbation thickness variations
6	$-q^2 h_0^3 G_{\xi\xi}$	Capillary flow in ζ direction induced by perturbation curvature in ξ
7	$q^4 h_0^3 G$	Capillary flow in ζ direction induced by perturbation curvature in ζ

applied perturbation. The mechanical energy of the disturbance is defined as an inner product of the disturbance film thickness according to

$$E = \frac{1}{2}\int_{-\infty}^{+\infty} (h_1)^2 d\xi = \frac{1}{2}\langle h_1, h_1\rangle. \qquad [31]$$

Recasting the linear equation [29] in terms of the full expression for h_1 yields the compact operator form

$$h_{1t} + L_{h_0}[h_1] = 0, \qquad [32]$$

where the linear operator L_{h_0}, which depends on the base flow solution, includes all of the terms with spatial derivatives in Eq. [29]. Calculating the rate of energy production, $dE/dt = \langle h_1, \dot{h}_1\rangle$, by taking the inner product of Eq. [32] with h_1 yields

$$\frac{dE}{dt} = \beta\langle G, G\rangle = -\langle G, L_{h_0}[G]\rangle. \qquad [33]$$

The dimensionless normalized rate of energy production, $\dot{E}_{\text{tot}}$, is therefore calculated to be

$$\beta = \dot{E}_{\text{tot}} = -\frac{\langle G, L_{h_0}[G]\rangle}{\langle G, G\rangle}. \qquad [34]$$

The operator L_{h_0} consists of seven terms, described in Table 1, each corresponding to a particular convective term in the overall flow. In Figs. 7 and 8 we have plotted for two different values of the precursor film thickness the contribution to the energy production rate from each term, $n = 1, \ldots, 7$, listed in Table 1, namely,

$$\dot{E}_n = -\frac{\langle G, L_{h_0,n}[G]\rangle}{\langle G, G\rangle}. \qquad [35]$$

Terms with positive values of $\dot{E}_n$ destabilize the flow while terms with negative values of $\dot{E}_n$ stabilize the flow.

We have studied the partitioning of energy among the different flow contributions for a large range of disturbance wavenumbers and several values of the precursor film thickness. Typical results of our studies are plotted in Fig. 7 for $b = 0.01$ and Fig. 8 for $b = 0.10$. By definition, the sum of all contributions for each value of q equals the eigenvalue $\beta(q)$. As observed in all cases studied, the inner product of h_1 with term 4 in Table 1 yields the largest destabilizing term. This term, labeled 4 in Figs. 7 and 8, reflects contributions to Marangoni flow in the streamwise direction created by regions in the flow where the local film thickness increases as a result of the applied perturbation. This enhanced mobility is by far the largest contributor to unstable flow. This same effect occurs in other driven spreading problems such as spin coating (9) in which regions of the flow which are locally thickened by the perturbation experience a higher mobility and therefore travel faster than neighboring thinner regions, thereby destabilizing the initially uniform front. As expected, the thicker the precursor film, the smaller the magnitude of this destabilizing term. Term 6 in Figs. 7 and 8 reflects a Rayleigh-like fluid redistribution, in which curva-

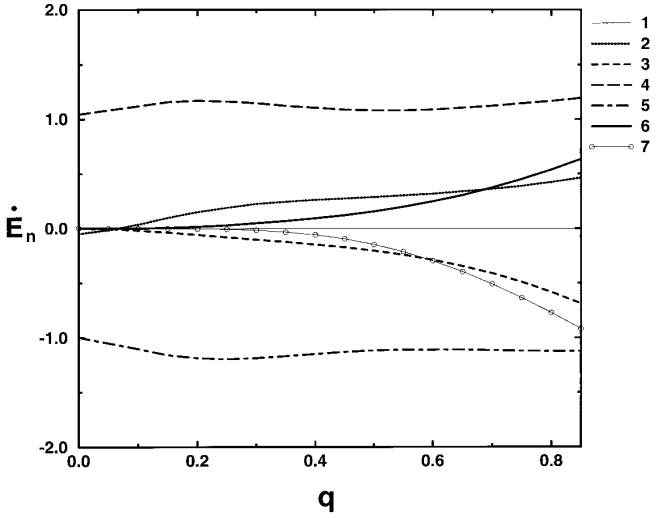

FIG. 7. Contribution to energy production of each term in the disturbance equation for a dimensionless precursor thickness of $b = 0.01$.

ture in the streamwise direction pumps fluid from the thinner portions of the film with higher Laplace pressures to thicker portions of the film with lower Laplace pressures. As in the breakup of a liquid jet, this type of term is destabilizing, but in this case not nearly so much as the Marangoni term. In fact, since the most destabilizing mode occurs around $q \approx 0.35$, this term hardly contributes to the instability of the capillary ridge. Term 7 is, of course, always stabilizing. This term corresponds to the second type of Rayleigh-like term in fluid jets, in which curvature in the transverse direction redistributes fluid from the thicker portions of the film with negative curvature to the thinner portions of the film with positive curvature. Term 1 does not affect the stability of the flow since it merely reflects the change in reference frame velocity to that of a traveling wave with nondimensional velocity $c = 1 + b$. Terms 3 and 5 are also stabilizing since capillary terms are here diminishing the change in the curvature of the rim in both the streamwise and transverse directions, thereby flattening the film and reducing the local mobility. The effect of term 2 for thin precursor films is somewhat surprising. Apparently for thin enough precursor films in which the perturbation G can assume a very steep advancing front and narrowed width, the Laplace pressure acts to further thicken the already thick portions of the capillary ridge. It would be interesting to explore extremely small values of the precursor film thickness to determine if term 2 can eventually overtake the destabilizing mechanism inherent in term 4. As plotted in Fig. 4a, though, for wave vectors close to $q_{max} \approx 0.35$, the sum total of contributions produces unstable flow caused mainly by the increased mobility in already thick portions of the spreading front.

DISCUSSION AND COMPARISON WITH EXPERIMENTS

Three different groups have so far studied the spreading behavior of thermally driven thin liquid films in either a vertical or horizontal geometry. In each case, the choice of substrate ensured complete wetting by the spreading fluid. Ludviksson and Lightfoot (1) examined the climbing of a squalane film along a vertical polished silver wafer partly submerged in a reservoir of squalane. Cazabat *et al.* (2, 3) used this same geometry to study the climbing behavior of a silicone oil film on a polished silicon wafer. Brzoska *et al.* (4) chose instead to study the horizontal spreading behavior of a small square patch of silicone oil on a polished silicon wafer in which the total fluid volume was finite. We discuss next the different results produced by these three groups and compare each with our theoretical predictions.

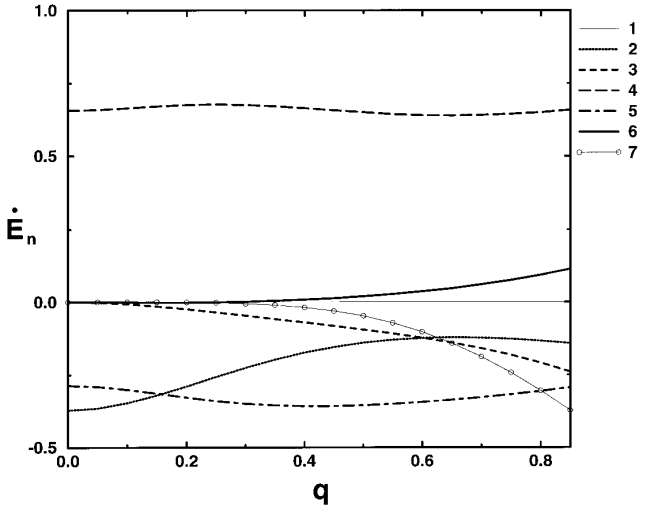

FIG. 8. Contribution to energy production of each term in the disturbance equation for a dimensionless precursor thickness of $b = 0.10$.

TABLE 2
Results for Vertically Spreading Films Examined by Ludviksson and Lightfoot (1)

h_{exp} (μm)	η (poise)	τ (dyn/cm^2)	$\tau/\rho g$ (μm)	U_{exp} (μm/s)	U_{mar} (μm/s)
0.94	0.31	0.090	1.1	0.0531	0.14
1.30	0.39	0.095	1.2	0.0333	0.16
1.40	0.36	0.11	1.4	0.0714	0.22
1.78	0.27	0.14	1.8	0.139	0.46
2.16	0.27	0.15	2.0	0.178	0.61
2.35	0.27	0.19	2.5	0.249	0.84
2.25	0.23	0.19	2.5	0.271	0.97

Note. The listed theoretical velocities, U_{mar}, were determined by Eq. [12].

Ludviksson and Lightfoot designed perhaps the most careful experiments in that they ensured a truly linear temperature profile along the direction of the climbing film by sandwiching several thermistors between two highly conducting silver plates. The temperature profile achieved was linear to within 5%. The squalane used was purified by molecular fractionation and chromatographic removal of polar contaminants by Florisil. For the temperature gradients used in their studies, the squalane spread vertically with a straight and uniform front. Ahead of the nominal contact line, a precursor film was detected which was believed to be drawn from the climbing film by surface diffusion. Interferometric measurements could only resolve the maximum thickness of this precursor film, which was estimated to be about 0.05 μm thick. In Fig. 10 of Ref. (1) is plotted the film thickness profile as observed by interferometry. At the leading edge, the film profile decreases monotonically toward the substrate with no indication of a capillary ridge. To understand this behavior, we have tabulated in Table 2 the relevant data from these experiments including the film thicknesses and climbing rates. As seen in column 4 of Table 2, the experiments by Ludviksson and Lightfoot are outside the regime for which our model holds since $h \sim \tau/\rho g$. If the flow were strictly driven by Marangoni stresses, with no drainage terms present, the velocities for the climbing films would be comparable to the values shown in the last column. It is clear that the experimental values are much smaller. Calculations

of the average velocity U including both Marangoni and drainage terms as calculated from Eq. [6] yield velocity estimates very close to those measured experimentally. Interestingly, Ludviksson and Lightfoot did mention in their work that after gravitational draining effects had ceased and a constant shape for the spreading front was established, they observed somewhat jagged and lobar forms at the spreading front, in which some parts of the front traveled faster than others. They observed these ''fingers'' only for the higher spreading rates but did not pursue further the details of the instability.

The fact that the thicker films failed to display any instability at the advancing front may be related to the absence of a pronounced capillary ridge or the absence of significant curvature in the film thickness profile in this region. It is interesting to note that in our stability calculations for thin films in which drainage is negligible, increasing the precursor film thickness decreases the amplitude and curvature of the capillary ridge, which in turn promotes stable and uniform flow. For precursor films $b > 0.50$, our numerical profiles for h_0 display just a small oscillation in film thickness at the advancing front and yield perfectly uniform flow. In future studies, we would like to explore situations in which the capillary ridge is prevented from forming by studying thicker films for which drainage is significant.

Cazabat *et al.* conducted two separate studies (2, 3) of light, nonvolatile silicone oil films (polydimethylsiloxane) climbing along a polished silicon wafer covered with a natural oxide which the silicone oil wets completely. Unfortunately, there was no check on the linearity of the temperature profile generated by placing the ends of the wafer in contact with two temperature controlled metal blocks, nor were the oils purified to prevent surface contaminants from further contributing to Marangoni flow from concentration variations. The spreading films were observed through a reflection microscope with laser illumination from a He–Ne laser. The films advanced vertically along the wafer and after several minutes displayed a capillary ridge, as shown in the profile reconstructions from interferometry in Fig. 9, and lateral undulations which eventually grew into long slender rivulets, as shown in Fig. 1.

We have tabulated in Table 3 the relevant measurements and theoretical estimates for these spreading films. As can be seen by comparing the experimental thicknesses in the second column with the ratio $\tau/\rho g$, the films in this study were certainly thin enough for drainage terms to be neglected. The discrepancies between the measured velocities and the theoretical predictions may be due to the combined uncertainty in the measurements of the stress τ and the film thickness. The stress was measured indirectly by estimating the temperature gradient along the wafer. The characteristic film thicknesses were measured far from the advancing front but not right behind the capillary ridge where $h = h_N$. Finally, the theoretical estimate for the climbing film due to Marangoni stresses assumes that no other forces in the outer region affect the fluid flux up the plate. In fact, for the experimental geometry used in Refs. (2, 3), it was observed that the high curvature in the meniscus region of the reservoir may also have affected the flow near the leading edge. This high curvature is clearly evident at the base of the wafer in the first photograph in Fig. 1. High meniscus curvatures could cause capillary forces to be significant everywhere, not just in the inner region as assumed by the model. Two recent studies have estimated the effects of meniscus curvature on the thickness of climbing films (3, 18). These studies show that it is the curvature of the reservoir meniscus which determines the thickness of the film in the outer region. The theoretical analysis, however, only examines the effects of curvature in the outer region and their influence on the unperturbed film thickness.

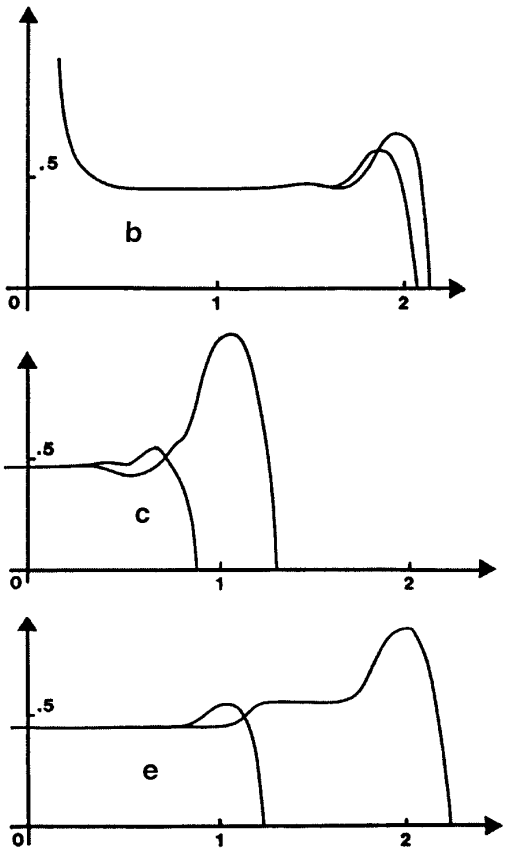

FIG. 9. Film thickness profiles corresponding to the photographs in Fig. 1. The two curves in each graph correspond to the most and least advanced portions of the film. Reproduced from Ref. (19).

As for similarities between the experimental observations and predictions of the model, we note from the top photograph in Fig. 1 that the spreading film exhibits decaying oscillations away from the advancing front, a feature evident in the interferometric profile reconstructions shown in Fig. 9. This oscillatory behavior is predicted by the numerical solutions of Eq. [26] and is especially pronounced for small

TABLE 3
Results for Vertically Spreading Films Examined by Cazabat and Co-workers

Ref.	h_{exp} (μm)	η (poise)	τ (dyn/cm^2)	$\tau/\rho g$ (μm)	U_{exp} (μm/s)	U_{mar} (μm/s)	Λ_{exp} (μm)	l (μm)	Λ_{exp}/l
(2)	0.86	0.2	5.0	54	8*	10.7	600	27	22
(2)	0.65	0.2	2.7	29	3*	4.4	610	27	22
(2)	0.54	0.2	2.1	23	3	2.8	480	25	19
(2)	0.27	0.2	1.0	11	1	0.68	370	20	18
(2)	0.17	0.2	0.54	5.8	0.3	0.23	340	18	19
(2)	0.65	1.0	2.1	22	0.8	0.7	580	28	21
(2)	0.33	5.0	2.1	22	0.1†	0.07	340	18	19
(3)	0.11	0.2	0.46	4.9	0.12	0.13	350	15	23
(3)	0.23	0.2	0.67	7.2	0.23	0.39	370	22	17
(3)	0.34	0.2	0.97	10	0.73	0.82	430	25	17
(3)	0.68	0.2	1.29	14	2.2	2.2	640	36	18
(3)	1.08	0.2	1.46	16	5.0	3.9	790	47	17
(3)	1.64	0.2	1.87	20	8.9	7.7	1160	58	20
(3)	1.98	0.2	2.12	23	12.6	10.5	1240	63	20

Note. The asterisks (*) denote measurements for which the linear regime was too short and a dagger (†) denotes data for which the slope was not sufficiently constant to give a precise reading.

values of b. In Table 3 we have also tabulated Cazabat *et al.*'s experimental values for the wavelength of the instability (measured from finger tip to tip) and compared these with our theoretical estimates. The average over all of the measurements taken gives a dimensionless value for the most unstable wavelength $\Lambda/l \approx 19.4$ (or 19.0 if the unreliable measurements indicated are removed). This is in excellent agreement with our prediction of $\Lambda/l \approx 18$ from the linear stability analysis for our thinnest precursor films. This agreement seems almost too good given the larger discrepancies discussed above. The reason for the excellent agreement is probably due to the fact that the inner length scale, $l \sim h_N^{2/3}\tau^{-1/3}$, which sets the wavelength of the instability, is less sensitive to the values of h_N and τ because of the fractional powers involved. As observed in Fig. 1 or Fig. 9, the protrusions at the advancing front form the thickest regions of the leading edge, in qualitative agreement with our predictions that the thicker portions advance the fastest. The mobility increase experienced by the thicker portions of the front is responsible for the overall destabilization of the spreading film.

Brzoska *et al.* (4) examined the spreading of a light silicone oil on a horizontal substrate resting on two aluminum blocks held at different temperatures. The focus of this study was to investigate in more detail the linear stability regime for which the fingering regions should grow exponentially in time. The oils used were not purified to prevent surface contaminants from further contributing to Marangoni flow from concentration variations. Nine small platinum thermocouples placed along the surface of the wafer were used, however, to monitor the temperature profile in the streamwise direction, which was found to be quite uniform. Instead of using a large reservoir of fluid, these studies investigated the spreading behavior of a finite strip of silicone oil. The fluid strip was applied by rolling a glass rod across a horizontal line of oil droplets to produce a liquid mound which was allowed to relax further by capillary forces. The temperature gradient was only then applied to the liquid strip to cause it to spread in the direction of the colder block. Since the film thicknesses created by the spreading mound were much larger than those achieved in previous experiments and since the applied temperature gradient was much smaller, the effective fingering wavelength was much larger and could be visualized with a standard CCD video camera. Various experimental and theoretical estimates are listed in Table 4. The film thickness, h_{exp}, was estimated before the application of any thermal gradient by weighing the wafer with the relaxed silicone oil strip and assuming a rectangular volume of fluid. This film thickness, h_{exp}, is therefore not related to the film thickness, h_N, used as a parameter in the model. The estimated Marangoni velocities shown in the seventh column, U_{mar}, were calculated using this initial film thickness, h_{exp}. Since there were no measurements of the liquid spreading rates reported by Brzoska *et al.*, we could not conclude whether these films were strictly thermally driven. Nonetheless, the values reported for h_{exp} satisfy the inequality $h\epsilon = h^2/L_c \ll \tau/\rho g$, thus ensuring that hydrostatic terms can be neglected and our analysis applied to these systems. The spreading films of Brzoska *et al.* were found to exhibit a capillary ridge and to undergo a fingering instability with an average dimensionless wavelength $\Lambda/l \approx 22.6$. This agreement is fairly close to the theoretical prediction of $\Lambda/l \approx 18$ for films with $b = 0.01$, especially given that the experimental film thickness used for this estimate was not h_N, but the estimated film thickness h_{exp}. The estimated film thickness yields a larger value of Λ/l, as expected.

TABLE 4
Results for Horizontally Spreading Films Examined by Brzoska *et al.* (4)

h_{exp} (μm)	h^2/L_c (μm)	η (poise)	τ (dyn/cm^2)	$\tau/\rho g$ (μm)	U_{mar} (μm/s)	Λ_{exp} (μm)	l (μm)	Λ_{exp}/l
1.54	0.00024	0.48	0.35	3.7	0.55	2300	98.2	23.4
3.3	0.0011	0.48	0.35	3.7	1.19	3600	162.6	22.1
6.3	0.0040	0.48	0.35	3.7	2.27	6000	250.7	23.9
7.3	0.0053	0.48	0.35	3.7	2.63	5900	276.7	21.3
9.0	0.0081	0.48	0.35	3.7	3.24	7400	318.6	23.2
16.0	0.026	0.48	0.35	3.7	5.76	10000	467.2	21.4

Note. The values for h^2/L_c were calculated using a characteristic length L_c of 1 cm. The actual characteristic length may have varied from run to run, but was not reported in (4).

The linear stability analysis presented can easily be extended to the location of the contact line in a manner similar to a previous stability analysis for gravitationally driven flows (8). Within this earlier framework, the growth of the sinusoidal shape of the advancing front can be tracked and compared directly with theoretical predictions. For very short times after the onset of unstable flow, the dimensionless peak to valley distance should grow as $L_{pv} \sim \exp(\beta t)$, where β is the dimensionless growth rate and t the dimensionless time. Both Cazabat and co-workers and Brzoska *et al.* measured L_{pv}, but the two groups observed different growth laws. Cazabat *et al.* found that once the instability formed both the peaks and valleys advanced linearly in time (2) whereas Brzoska *et al.* measured exponential growth (4). Both sets of measurements, however, included data beyond the linear regime since the measurements were made on fingers whose shape exceeded a simple sinusoidal form. More extensive early time data are necessary to determine the actual growth rate of the advancing front. Nonetheless, comparing the value of Brzoska *et al.*'s parameter, $m = 6.4 \pm 0.4$, for the rise time of the instability to our theoretical estimate for the growth rate, $(\beta(q_{max}))^{-1} = 9.1$ for $b = 0.01$, gives reasonable agreement. Smaller values of b would yield slightly larger values of β, further improving agreement between experiments and theoretical predictions. Further studies of this sort designed to explore the detailed predictions of linear stability theory would go a long way in helping confirm or improve the theoretical modeling, as would more careful measurements of the precise shape and velocity of the unperturbed films on both thick and thin precursor films.

SUMMARY

We have analyzed the spreading behavior of nonvolatile thermally driven films by separately investigating the outer region, in which Marangoni stresses balance viscous stresses, and the inner region, which includes these two forces as well as capillarity. The outer region admits a simple self-similar form, $h = \eta x/\tau t$, where x represents the direction of spreading, τ is the thermally induced constant surface stress, and t is time. The leading edge of this linear ramp ends abruptly at a height, h_N, which must smoothly match onto the substrate by bending the film profile. The inner region in which the capillary forces become comparable to viscous and Marangoni forces is determined by scaling analysis to be of length $l = h_N(3Ca)^{-1/3}$ when the capillary number is based on the velocity of the fluid at the entrance to the inner region, namely $U_{mar}(h_N)$. The equation for the inner region resembles other third-order equations describing driven spreading problems and assumes shapes ranging from films with a pronounced capillary ridge at the advancing front to films with a simple monotonically decreasing thickness, depending on the thickness of the precursor film assumed.

The linear stability of these numerical profiles indicates a strong correlation between the stability and the shape of the unperturbed profiles. In particular, films with a pronounced ridge and high front curvature are very unstable to perturbations at the leading edge, while films which are relatively featureless and flat close to the leading edge produce stable and uniform spreading. Comparison with results from several groups indicates that the unperturbed and disturbance equations accurately capture many features of the experimental profiles, including good agreement with the film thickness profile and the most unstable wavelength, as well as the magnitude of the growth rate displayed by the rivulets formed. The energy analysis for such thermally driven flows illustrates that the main cause of the instability is directly related to the increased mobility experienced by thicker portions of a disturbed film. The corresponding shape assumed by the unstable profiles closely resembles the experimentally observed profiles.

According to our analysis, it appears that substrates requiring a stable uniform coating should first be precoated with a layer of liquid at least one quarter the thickness of the film to the coated. This would prevent the formation of a capillary ridge, yield a flatter coating, and discourage any rivulet formation at the leading edge. As described earlier, it would

be interesting to study the effects of drainage on thermally driven films to deduce whether this additional effect could also prevent the formation of a bulge at the advancing front. The results from the experiments of Ludviksson and Lightfoot certainly suggest the use of drainage as an alternative mechanism for eliminating unstable flow.

APPENDIX: NOMENCLATURE

A Cross sectional area of fluid in x–z plane
a Iteration parameter in numerical solution of base flow
b Dimensionless precursor film thickness
c Dimensionless velocity of traveling wave
Ca Capillary number
E Energy
$\dot{E}_n$ Dimensionless normalized rate of energy production of term n
$\dot{E}_{\mathrm{tot}}$ Dimensionless normalized rate of energy production
G Dimensionless disturbance function for streamwise part of the flow
g Gravity constant
h Film thickness
h_0 Dimensionless base flow film profile
h_1 Full dimensionless disturbance function
h_{c} Characteristic film thickness
h_{exp} Experimental film thickness
h_N Film thickness at leading edge of outer region
l Inner region length scale
L_{c} Characteristic extent of film in outer region (streamwise and transverse directions)
L_{h_0} Linear disturbance operator
L_{pv} Dimensionless peak to valley distance
m Brzoska *et al.*'s growth parameter
n Term index
p Pressure
p_{cap} Capillary pressure
q Dimensionless disturbance wavenumber
q_{max} Most unstable wavenumber
T Temperature
t Time
U Height-averaged velocity in streamwise direction
u Local velocity in streamwise direction
U_{exp} Experimentally measured velocity
U_{mar} Marangoni velocity
U_N Height-averaged velocity in streamwise direction evaluated at h_N
V Height-averaged velocity in transverse direction
v Local velocity in transverse direction
x Streamwise coordinate
x_* Initial value of characteristic
x_N Location of film front in analysis of outer region
y Transverse flow coordinate
z Coordinate perpendicular to substrate

Greek Symbols

α Constant given by $(1 - b)^{1/3}/2$
β Dimensionless disturbance growth rate
γ Local surface tension
$\Delta\gamma$ Characteristic change in surface tension
ϵ Lubrication parameter denoting $h_{\mathrm{c}}/L_{\mathrm{c}}$
ζ Dimensionless transverse flow coordinate
η Viscosity
Λ Wavelength of fingering instability measured tip to tip
Λ_{exp} Experimental wavelength of fingering instability measured tip to tip
ξ Dimensionless streamwise coordinate
ρ Density
τ Surface shear stress induced by thermal gradient

ACKNOWLEDGMENTS

The authors gratefully acknowledge support from the National Science Foundation through a graduate fellowship (DEK), a Research Initiation and CAREER award (SMT), and a MRSEC seed grant (SMT).

REFERENCES

1. Ludviksson, V., and Lightfoot, E. N., *AIChE J.* **17,** 1166 (1971).
2. Cazabat, A. M., Heslot, F., Troian, S. M., and Carles, P., *Nature* **346,** 824 (1990).
3. Carles, P., and Cazabat, A. M., *J. Colloid Interface Sci.* **157,** 196 (1993).
4. Brzoska, J. B., Brochard-Wyart, F., and Rondelez, F., *Europhys. Lett.* **19,** 2 (1992).
5. Levich, V. G., ''Physicochemical Hydrodynamics.'' Prentice Hall, Englewood Cliffs, NJ, 1962.
6. Deryagin, B. V., Strakhovskii, G., and Malysheva, D., *Zh. Eksp. Teoret. Fiz.* **16,** 171 (1946).
7. Deryagin, B. V., Kusakov, M. M., and Krym, K. S., *Zh. Eksp. Teoret. Fiz.* **16,** 179 (1946).
8. Troian, S. M., Herbolzheimer, E., Safran, S. A., and Joanny, J. F., *Europhys. Lett.* **10,** 25 (1989).
9. Spaid, M. A., and Homsy, G. M., *Phys. Fluids* **8,** 460 (1996).
10. Huppert, H. E., *Nature* **300,** 427 (1982).
11. Moriarty, J. A., Schwartz, L. W., and Tuck, E. O., *Phys. Fluids* **3,** 733 (1991).
12. Hocking, L. M., *J. Fluid Mech.* **76,** 801 (1976).
13. Greenspan, H., *J. Fluid Mech.* **84,** 125 (1978).
14. Friz, V. G., *Z. f. Angew. Physik* **19,** 374 (1965).
15. Tanner, L. H., *J. Phys. D.* **12,** 1473 (1979).
16. Tuck, E. O., and Schwartz, L. W., *SIAM Rev.* **32,** 453 (1990).
17. Smith, B. T., ''Matrix Eigensystem Routines–EISPACK Guide,'' 2nd ed., Vol. 6 of Lecture Notes in Computer Science, Springer-Verlag, New York, 1976.
18. Fanton, X., Cazabat, A. M., and Quéré, D., *Langmuir* **12,** 5875 (1996).
19. Cazabat, A. M., Heslot, F., Carles, P., and Troian, S. M., *Adv. Colloid Interface Sci.* **39,** 61 (1992).